

Field-tunable spin disordered phase in the triangular-lattice delafossite TiYbSe_2

Bishnu P. Belbase^{1,*}, Arjun Unnikrishnan^{1,2,*}, Eun Sang Choi³, and Arnab Banerjee^{1,†}

¹ *Department of Physics and Astronomy, Purdue University, West Lafayette, Indiana 47906, USA*

² *Solid State and Structural Chemistry Unit (SSCU),*

Indian Institute of Science, Bengaluru - 560012, India and

³ *National High Magnetic Field Laboratory, Tallahassee, Florida - 32310, USA*

We introduce a relatively disorder-free frustrated triangular lattice compound TiYbSe_2 belonging to the rare-earth delafossite family - extending the search for the quintessential chiral quantum spin liquid state. While DC magnetization suggests magnetic exchange interactions in the order of several kelvin, the zero-field AC magnetization and heat capacity measurements reveal no signs of long-range magnetic order down to 20 mK, indicating a highly frustrated quantum-disordered ground state. The high-field AC magnetization reveals a phase diagram generally consistent with a large family of Yb delafossites. We observe a spin glass transition around ~ 30 mK at zero field, which we argue is due to free spins. A broad anomaly in the heat capacity measurements between 2 – 5 K - indicative of short-range spin correlations - along with a linear temperature dependence at low temperatures and the complete absence of long-range order at low fields, establishes the low-temperature, low-field regime of TiYbSe_2 as a prime location for exploring field-tunable QSL behavior.

I. INTRODUCTION

In the decades since Anderson's theory, the search for real materials exhibiting quantum spin liquid (QSL) behavior has become a central focus in condensed matter physics [1–6]. QSLs are often realized in low-dimensional magnetic systems with geometrically frustrated lattices, such as triangular, kagome, or honeycomb structures [7–15]. Among these, the two-dimensional (2D) triangular lattice stands out as one of the simplest yet most versatile platforms for hosting exotic quantum magnetic ground states, including the elusive QSL.

Recently rare-earth-based triangular lattice materials, where the strong spin-orbit coupling (SOC) and crystal electric field (CEF) effects introduce additional complexity and richness to the magnetic interactions, have become popular [16, 17]. While the absence of long-range order (LRO) down to 0.4 K or lower has been attributed to QSL behavior, the conclusion of the presence of a true QSL phase is confounded by the alternative scenarios which have been hard to preclude, such as the effect of disorders [18], a spin-glass state [19], random singlet phase [20], or a magnetic order at a much lower temperature [21]. Within this class of materials, Yb^{3+} -based delafossites have emerged as particularly attractive due to their ideal 2D triangular lattice geometry and the effective spin-1/2 state of Yb^{3+} ions. The delafossite family, with the general formula AYbX_2 (where A is a monovalent metal ion and X is a chalcogen such as O, S, Se, or Te), offers a clean and a relatively disorder-free platform for studying frustrated magnetism. By tuning the A -site cation or the chalcogen X , one can systematically control interlayer and intralayer interactions, en-

abling the exploration of novel quantum magnetic ground states [22, 23]. Recently, some candidates of the family AYbX_2 have already been extensively studied and shown to exhibit proximate QSL phases [24–37], including a potential gapped \mathbb{Z}_2 spin liquid state [27] which can host abelian anyons [38] with strong signs of criticality and entanglement.

In this work, we introduce a thallium-based variant of the delafossite family, TiYbSe_2 , by substituting Tl^+ at the A -site. The larger ionic radius of Tl^+ compared to Na^+ and K^+ is expected to further reduce interlayer interactions, thereby enhancing quantum fluctuations and potentially stabilizing a QSL ground state easily. We have synthesized and investigated TiYbSe_2 using DC and AC magnetization measurements, as well as heat capacity studies, down to ultralow temperatures. Our results reveal the absence of magnetic LRO down to 20 mK, but a frequency-dependent peak in the zero-field susceptibility near 30 mK indicates the emergence of a glassy phase at very low temperatures—likely arising from orphan spins and, to the best of our knowledge, a temperature regime previously unexplored for glassy transitions in this family of materials. We observe a field-induced magnetic LRO above 3 T, as is universally observed in isostructural systems and predicted by theoretical models. Importantly, the low-temperature heat capacity data exhibit a broad maxima between 2 – 5 K, indicative of short-range correlations and a quantum-disordered ground state. Upon subtracting the nuclear and phonon contributions, it is found that the heat capacity below 350 mK follows a linear temperature dependence. Taken together with the complete absence of an LRO, our results point to a gapless spin liquid state in TiYbSe_2 . We propose that the phases below 350 mK at low fields (below 2 T) offer promising regimes for exploring QSL physics.

* These authors contributed equally to this work

† arjunu@iisc.ac.in

‡ arnabb@purdue.edu

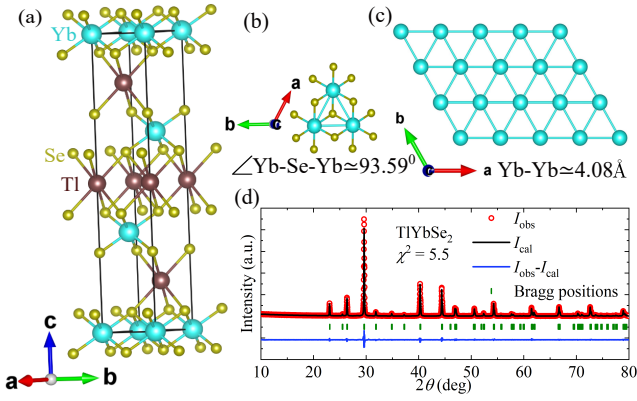


FIG. 1. **Crystal structure and powder X-ray diffraction (XRD) of TIYbSe₂.** (a) 3D crystal structure. (b,c) 2D plane showing a triangular layer of magnetic Yb atoms with Yb-Yb bond length and $\angle \text{Yb-Se-Yb}$ bond angle. (d) Powder XRD pattern with Le Bail fit indicating the phase purity of the synthesized samples.

II. RESULTS AND DISCUSSIONS

A. Synthesis and crystal structure

Polycrystalline samples of TIYbSe₂ were synthesized via the solid-state reaction method using thallium (Tl) granules (99.99%, Thermo Fisher), ytterbium (Yb) powder (99.9%, Thermo Fisher), and selenium (Se) powder (99.999%, Thermo Fisher) mixed in appropriate ratios and maintained at 800 °C for 72 hours yielding a black powder. The non-magnetic analog TlLuSe₂, used as a reference for phonon heat capacity, was synthesized following an identical procedure using lutetium (Lu) powder (99.9%, Thermo Fisher) instead of Yb powder.

The phase purity of the samples was confirmed through powder X-ray diffraction (XRD) measurements performed at room temperature using a PANalytical Empyrean diffractometer equipped with an incident beam monochromator and Cu K α radiation. The Le Bail profile fit of the obtained XRD data was performed using the FullProf package [39]. The fitting was carried out using the trigonal $R\bar{3}m$ (No. 166) space group, with initial parameters taken from Ref. [40] [see Fig. 1(d)]. The goodness of fit is $\chi^2 \simeq 5.5$. The obtained lattice parameters are $a = b = 4.0780(1) \text{ \AA}$, $c = 23.1387(1) \text{ \AA}$, $\alpha = \gamma = 90^\circ$, $\beta = 120^\circ$, and $V_{\text{cell}} = 333.25(1) \text{ \AA}^3$. These values are in close agreement with the reported values [40].

TIYbSe₂ crystallizes in a delafossite-type structure. The structure comprises two-dimensional (2D) triangular layers of Yb ions, separated by Tl layers, as shown in Fig. 1(a). Within the ab -plane, Yb ions form edge-sharing distorted octahedra with selenium, referred to as YbSe₆ octahedra, depicted in Fig. 1(b). The Yb-Yb distance in a triangular layer is $\sim 4.08 \text{ \AA}$. The unit cell contains three Yb layers stacked along the c -axis, with

an interlayer Yb-Yb distance of $\sim 8.06 \text{ \AA}$, which is significantly larger than that of most well-studied delafossites due to the larger size of Tl⁺ ions [22, 24–26].

B. DC magnetization

To understand the nature and strength of magnetic exchange interaction, DC magnetization measurements down to 1.8 K were performed using a Quantum Design SQUID-based magnetometer (MPMS-3), at the Birck Nanotechnology Center user facility at Purdue University. Fig. 2(a) presents the temperature dependence of the inverse susceptibility, $1/\chi(T)$, measured under an applied magnetic field of 0.5 T. The corresponding $\chi(T)$ data is provided in Supplemental Material (SM) Fig. 5(a) [41]. No signature of magnetic LRO is observed down to 1.8 K.

At high temperatures ($T > 100 \text{ K}$), the $1/\chi(T)$ data exhibit linear behavior and can be described by a modified Curie Weiss (CW) law:

$$\chi(T) = \chi_0 + \frac{C}{(T - \theta_{\text{CW}})}. \quad (1)$$

Here, χ_0 represents the temperature-independent contribution, consisting of the diamagnetic susceptibility of core electron shells and van-Vleck paramagnetic susceptibility of the open shells of the Yb³⁺ ions, while the second term represents CW law. The parameters θ_{CW} and $C = N_A \mu_{\text{eff}}^2 / 3K_B$ correspond to the CW temperature and Curie constant, respectively, with N_A as Avogadro's number, K_B as Boltzmann's constant, and $\mu_{\text{eff}} = g\sqrt{J(J+1)} \mu_B$ as an effective moment where g is the Lande g -factor, μ_B is the Bohr magneton, and J is the spin quantum number. The $1/\chi$ data is fitted in the temperature range of 200 K to 300 K [see Fig. 2(a)], yielding $\chi_0 \simeq 5.6 \times 10^{-4} \text{ emu/mol.Oe}$, $\mu_{\text{eff}}^{\text{HT}} \simeq 5.1 \mu_B$ [which is close to the theoretical value of $4.54 \mu_B$ for free Yb³⁺ ions with $J = 7/2$ and $g = 8/7$], and $\theta_{\text{CW}}^{\text{HT}} \simeq -71 \text{ K}$. Below 100 K, $1/\chi(T)$ deviates from CW behavior, exhibiting a change in slope. This deviation likely arises from the thermal depopulation of excited crystal electric field (CEF) levels, indicating that the large magnitude of $\theta_{\text{CW}}^{\text{HT}}$ primarily reflects CEF effects rather than direct exchange interactions.

In Yb³⁺-based spin systems, the interplay of SOC and CEF effects typically results in a Kramers doublet ground state, where low-temperature magnetic properties can be effectively described by a $J_{\text{eff}} = 1/2$ ground state [25, 26, 42–46]. To achieve a more accurate estimation of the magnetic exchange at low temperatures, we fitted the data below 5 K using Eq. (1), as it remains linear in this regime [see inset Fig. 2(a)]. The deviation of data below 2.3 K is likely due to the onset of a broad maximum, arising from short-range correlations, as clearly observed in the specific heat capacity analysis. The fit yields $\chi_0 \simeq 6.9 \times 10^{-3} \text{ emu/mol.Oe}$, $\mu_{\text{eff}}^{\text{LT}} \simeq 2.6 \mu_B$,

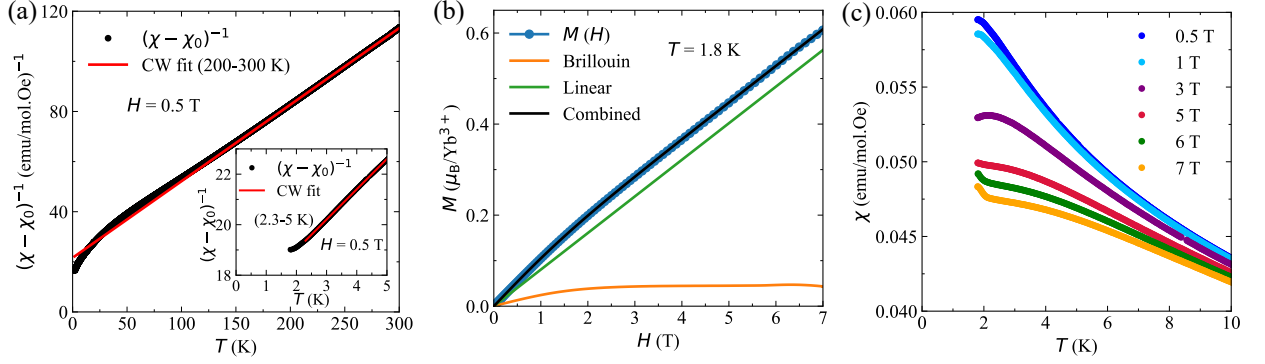


FIG. 2. **DC magnetization and magnetic susceptibility.** (a) Temperature-dependent inverse magnetic susceptibility ($1/\chi(T)$) at 0.5 T, with modified CW fit using Eq. 1 at high-temperature region. The corresponding $\chi(T)$ data (1.8 – 300 K) is provided in SM Fig. 5(a) [41]. Inset: low-temperature modified CW fit using Eq. 1. (b) Isothermal magnetization $M(H)$ at 1.8 K with two-component model (linear + Brillouin) fitting. (c) Temperature-dependent magnetic susceptibility measured at different applied fields.

and $\theta_{\text{CW}}^{\text{LT}} \simeq -13.8$ K. The extracted local moment corresponds to a $J_{\text{eff}} = 1/2$ state with a powdered averaged $g \simeq 3.0$. The magnetic entropy calculation in the following section further confirms the $J_{\text{eff}} = 1/2$ state. The large negative $\theta_{\text{CW}}^{\text{LT}}$ indicates dominant antiferromagnetic (AFM) exchange interactions. A simple estimation of the nearest-neighbor (NN) exchange coupling in a triangular lattice using $\theta_{\text{CW}} = -3J_1/2$ yields $J_1 \simeq 9.2$ K for TiYbSe_2 . Notably, the values of θ_{CW} and J_1 for TiYbSe_2 are higher than those of its isostructural counterparts [25, 26, 32, 33], indicating a stronger AFM exchange interaction. For instance, the J_1 value of TiYbSe_2 is more than twice that of NaYbSe_2 [26].

Isothermal magnetization $M(H)$ measurements at 1.8 K, is shown in Fig. 2(b). For a $J_{\text{eff}} = 1/2$ state with $g = 3.0$, the expected saturation magnetization is $1.5 \mu_B/\text{Yb}^{3+}$. However, measurements at 1.8 K up to 7 T were able to polarize only about one-third of the Yb moments, highlighting the strength of the exchange interactions. To estimate the fraction of free spins present in the system, the $M(H)$ data were fitted using a two-component model consisting of Brillouin-like free spins [47] and linear AFM exchange-field-bound moments [see Fig. 2(b)] using the expression [25, 48] $M = \chi H + f_{\text{fs}} N_A g_{\text{fs}} \mu_B J_{\text{fs}} B_{J_{\text{fs}}}(x)$, where χ is the intrinsic susceptibility of the sample, f_{fs} is the molar fraction of the free spins, N_A is the Avogadro's number, g_{fs} is the free spin g -factor, S_{fs} is the free spin, $B_{J_{\text{fs}}}(x)$ is the Brillouin function [47], and the modified argument of the Brillouin function is $x = g_{\text{fs}} \mu_B S_{\text{fs}} H / [k_B (T - \theta_{\text{fs}})]$. Comparing the saturation magnetization of free spins with the expected saturation magnetization of TiYbSe_2 suggests approximately 3% of the moments as free spins. We note that this number is much lower than that reported for NaYbO_2 [25].

Fig. 2(c) presents the magnetic susceptibility $\chi(T)$ measured down to 1.8 K at various applied magnetic fields. A broad maximum-like feature appears around

2 K at low applied fields and shifts to higher temperatures as the field increases. Above 6 T, an anomaly appears in $\chi(T)$, with an upturn below 2 K, hinting at a field-induced magnetic phase transition. To further investigate this behavior, AC magnetization measurements were conducted and are discussed in the following section.

C. AC magnetization

To better understand the low-temperature magnetic behavior and field-induced effects in TiYbSe_2 , we performed AC magnetization measurements at the National High Magnetic Field Laboratory (NHMFL) using an AC susceptometer at a frequency of 313 Hz and 1.7 Oe of AC field, equipped with a ^3He insert for measurements down to 300 mK. Zero-field frequency-dependent AC susceptibility measurements between 150 mK to 20 mK were done with a top-loading dilution refrigerator at 0.9 Oe of AC field.

Fig. 3(a) presents the real part of AC magnetic susceptibility, $\chi'(T)$, measured down to 0.3 K under different applied magnetic fields up to 3 T. At zero field, $\chi'(T)$ continues to diverge as the temperature decreases, indicating the absence of long-range magnetic ordering down to 0.3 K. With the application of a small magnetic field, the divergence in $\chi'(T)$ is suppressed, and a broad maximum emerges. The temperature corresponding to this maximum increases nearly linearly with the applied field, following the expected Zeeman splitting (ΔE) of isolated $J_{\text{eff}} = 1/2$ moments, given by $\Delta E = 2\mu_B g J_{\text{eff}} H$, where $g = 3.0$, obtained from low-temperature CW fitting. Such a broad maximum can arise from free Yb^{3+} moments, such as those present at grain boundaries of a polycrystalline sample, and is consistent with $M(H)$ data at 1.8 K which suggests that $\sim 3\%$ of the moments remain as free spins (see DC magnetization section). At 3 T, the broad maximum nearly disappears, and $\chi'(T)$

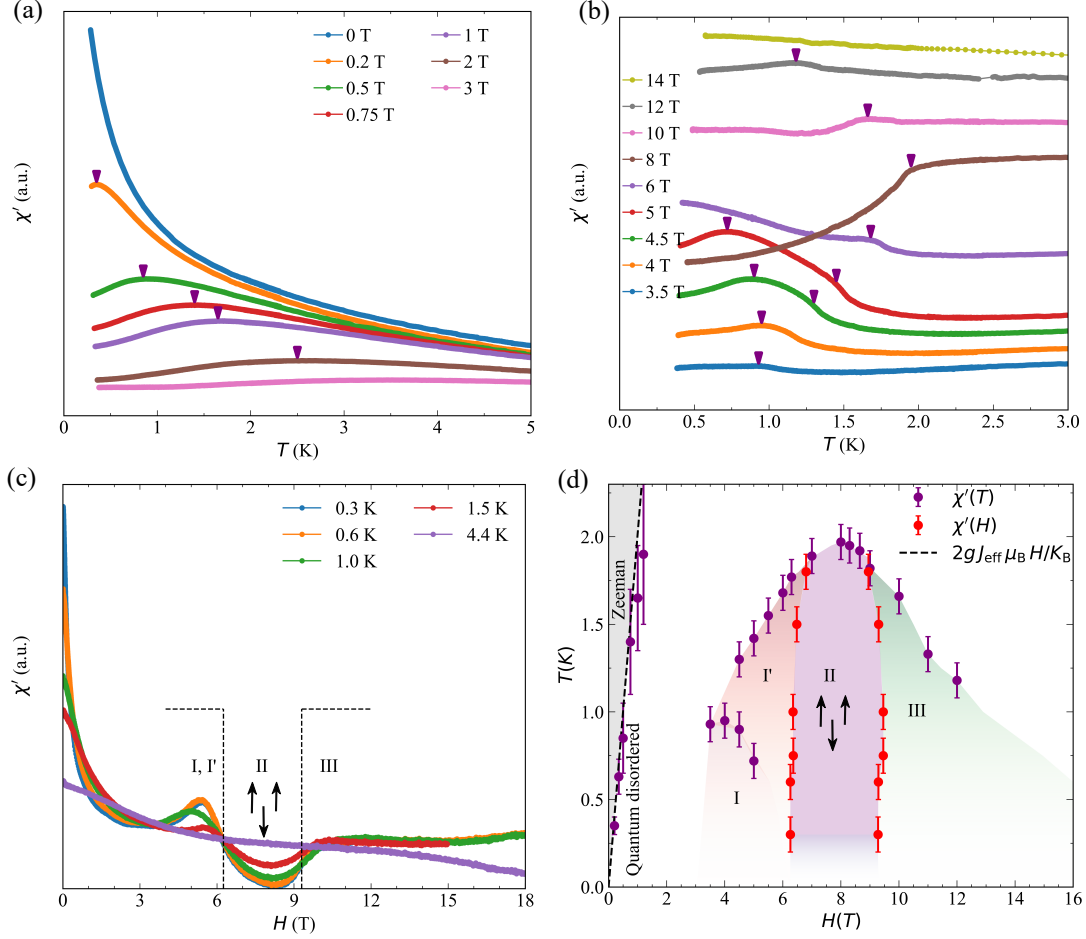


FIG. 3. AC magnetic susceptibility. (a) $\chi'(T)$ measured at low magnetic fields (0 T to 3 T). Purple arrows mark the broad maxima at different fields. (b) $\chi'(T)$ measured at high magnetic fields (3.5 T to 14 T), where the system is in a magnetically ordered state. Each curve is vertically offset for clarity, with non-uniform shifts relative to the field. The original, unshifted data are provided in SM Fig. 6(b) [41]. Purple arrows indicate transition temperatures at different fields. (c) Field-dependent $\chi'(H)$ data measured at various temperatures. The dotted black lines denote phase boundaries discussed in the phase diagram. (d) The $H - T$ phase diagram of TiYbSe_2 constructed from $\chi'(T)$ and $\chi'(H)$ data. Purple and red solid circles indicate the anomalies in $\chi'(T)$ and $\chi'(H)$, respectively. The dashed line represents the Zeeman-driven quenching of a minority fraction of free Yb moments under an applied magnetic field. The field-induced ordered regime is divided into three phases: (I, I'), II, and III.

becomes almost temperature-independent, reflecting the response of the remaining bound Yb moments. A similar Zeeman contribution was observed in the $\chi'(T)$ data of isostructural compound NaYbO_2 , where $\sim 7\%$ free spins were reported[25].

With a further increase in the applied field, the system transitions into an ordered state, as shown in Fig. 3(b). By 14 T, the transition falls outside the measurement window. The isothermal AC magnetic susceptibility, $\chi'(H)$, presented in Fig. 3(c), provides further insight into the field-induced transitions. As the field increases, $\chi'(H)$ decreases, reaching a minimum around 3.5 T, where χ' becomes nearly temperature-independent. With further field increase, the susceptibility starts to rise again, reaching a maximum at ~ 5.5 T.

Beyond this field, $\chi'(H)$ continuously decreases, reaching another minimum around 8 T. This minimum coincides with the field at which the transition temperature in the ordered regime is maximized, as shown in Fig. 3(b). For fields above 8 T, $\chi'(H)$ begins to recover, indicating a higher-field phase boundary where transition temperatures shift toward lower values and move beyond the measurement window.

The phase diagram constructed from $\chi'(T)$ and $\chi'(H)$ measurements is shown in Fig. 3(d). As the magnetic field increases, the system transitions into a field-induced magnetic LRO regime, where distinct phases emerge as a function of the applied field. At low fields, the system enters into phases I and I', followed by a transition into phase II at ~ 6.3 T, which persists up to ~ 9.3 T. Be-

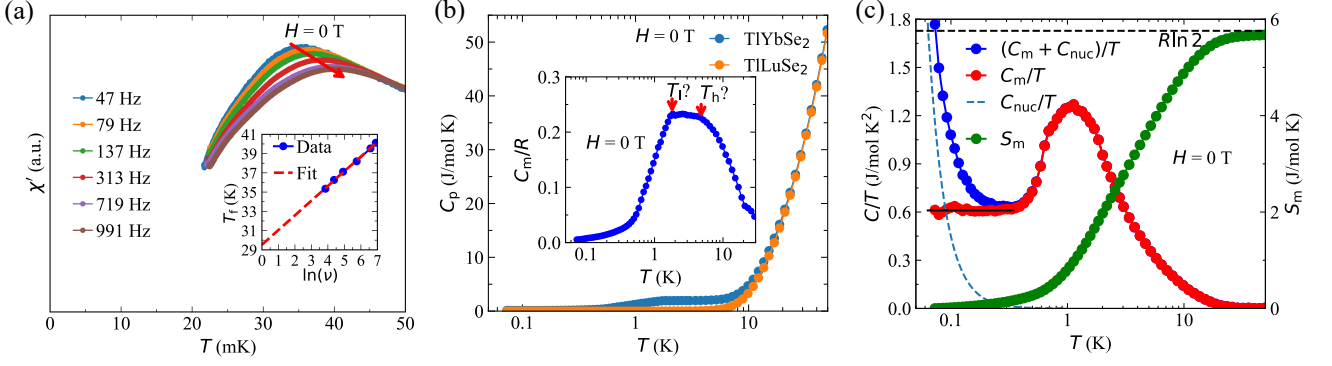


FIG. 4. **Sub-Kelvin AC magnetization and specific heat capacity.** **a** Frequency-dependent $\chi'(T)$ measured from 20 mK to 50 mK at zero field, showing signatures of spin glass transition, which we argue is due to free spins (y -axis starts from zero). The red arrow highlights the shift in the glassy transition temperature with frequency. The inset shows the dependence of the freezing temperature (T_f) on frequency (ν), with a red dashed line showing a linear fit to the data. The high temperature frequency-dependent $\chi'(T)$ is provided in SM Fig. S2a [41]. **b** The zero-field specific heat capacity, $C_p(T)$, of TiYbSe₂ measured down to 70 mK, overlaid with the phonon-only specific heat, $C_{ph}(T)$, of the non-magnetic isostructural analogue TlLuSe₂. Inset: Zero-field $C_m(T)$ normalized by the gas constant R (C_m/R) exhibits two broad maxima at approximately $T_l \simeq 2$ K and $T_h \simeq 5$ K. **c** Temperature-dependence of zero-field heat capacity divided by temperature, C/T (left y -axis), and the calculated magnetic entropy, $S_m(T)$ (right y -axis) as a function of temperature. The plotted heat capacity represents the contribution after subtracting the phonon contribution. The solid black line in C_m/T serves as a guide to the eye, highlighting the linear behavior of heat capacity. The black dotted line marks the value of $R \ln 2$ (right y -axis).

yond this field, the system transitions into another field-induced phase (Phase III), which persists up to the highest measured field.

Notably, the phase transitions observed in TiYbSe₂ closely resemble those reported in the isostructural compounds NaYbSe₂ and KYbSe₂ [26, 49]. In phase I and I', a 120° phase or an oblique 120° phase (Y-coplanar) may be stabilized. In an ideal triangular-lattice antiferromagnet (TLAF) described by the Heisenberg or XXZ Hamiltonian with nearest-neighbor exchange, two separate phases like I and I' are not typically expected. Their presence in TiYbSe₂ suggests the influence of additional next-nearest-neighbor magnetic interactions [49]. Phase II is expected to have an up-up-down (UUD) collinear spin structure, as indicated by the complete suppression of $\chi'(H)$. In TLAFs systems, UUD phases are characterized by a magnetization plateau at 1/3 of saturation magnetization (M_{sat}) [2, 50–52]. Experimentally, such UUD phases have been observed in several TLAF compounds [26, 49, 53–58]. Phase III has been proposed to correspond to a 2 : 1 canted phase [59]. As the field increases further, the spins are expected to fully align along the field direction, reaching the saturation magnetization, M_{sat} . Although the fully spin-polarized state lies beyond the measurement range of this study, the saturation field can be estimated based on the position of the UUD phase. In TLAF systems, full spin polarization generally occurs at approximately three times the field of the UUD phase [26, 55, 57]. This suggests that complete spin polarization in TiYbSe₂ likely occurs around 20 T, a significantly higher saturation field than in other members of this material family [25, 26, 49]. This finding

further supports the presence of enhanced AFM exchange interactions in TiYbSe₂.

The AC susceptibility measurements at zero-field extended down to 20 mK, as shown in Fig. 4a, reveal a peak around ~ 35 mK at a frequency of 47 Hz. This peak shifts to higher temperatures with increasing frequency (ν), a characteristic signature of a spin glass transition. A linear fit to the $\ln(\nu)$ versus freezing temperature (T_f) data, extrapolated to 1 Hz, yields a spin glass transition temperature of 29.5(2) mK. To the best of our knowledge, no previous AC susceptibility measurements below 50 mK have been reported for any of the compounds of the delafossite family to explore a possible glassy state. The spin glass transition at this low temperature is likely driven by the presence of free spins in the system, which we discuss in the next section.

Importantly, in the finite-field regime below 2 T and down to temperatures as low as 20 mK, it lacks the signatures of the 120° phase. As has been discussed for KYbSe₂ [24], the suppression of the 120° phase, indicative of quantum critical behavior and the onset of a possible QSL phase, forms a prime argument for the proximate QSL phase in that compound. Here, the absence of 120° phase in TiYbSe₂ is therefore significant and suggests that this low-temperature finite field regime could be a prime location for the search of QSL physics.

D. Specific heat capacity

To understand the nature of quantum disordered ground state, specific heat capacity measurements were

carried out using a physical property measurement system (PPMS, Quantum Design). Field-dependent specific heat capacity measurements down to 1.8 K were performed at the spin lab facility in the Birck Nanotechnology Center at Purdue University. The Zero-field data was collected using a dilution refrigerator insert, allowing measurements down to 70 mK at Quantum Design, San Diego.

Fig. 4(b) presents the zero-field specific heat capacity, $C_p(T)$, of TiYbSe_2 down to 70 mK, along with that of the non-magnetic analog TiLuSe_2 , which represents the phonon-only contribution, $C_{\text{ph}}(T)$. The difference, $C_p(T) - C_{\text{ph}}(T)$, accounts for the magnetic contribution to the specific heat capacity, $C_m(T)$, along with a nuclear Schottky contribution, $C_{\text{nuc}}(T)$, at very low temperatures ($T < 0.3$ K). The $C_m(T)$, is estimated by subtracting the $C_{\text{nuc}}(T)$ term, which is determined through fitting, as discussed later in this section. The $C_m(T)$ shows no evidence of magnetic LRO, consistent with the AC magnetic susceptibility measurements. A broad maxima in $C_m(T)$ is observed between 2–5 K [inset Fig. 4(b)], a characteristic feature of quasi-2D systems. This feature may signal a crossover into a QSL state. Notably, in related compounds such as NaYbO_2 and NaYbSe_2 , similar broad maxima arise from the superposition of two broad peaks, suggesting two distinct energy scales of exchange interactions [25, 26]. The emergence of such double broad maxima in $C_p(T)$ has been theoretically predicted for 2D triangular and kagome lattice antiferromagnets with a fully frustrated disordered ground state [60, 61]. Experimentally, similar behavior has been observed in several TLAF systems [25, 26, 62, 63]. For spin-1/2 TLAFs, the two crossover temperature scales are expected at $T_l/J = 0.2$ and $T_h/J = 0.55$ [64]. The broad maxima in TiYbSe_2 align closely with these predictions, given the exchange coupling $J = 9.2$ K obtained from CW fitting. Furthermore, for frustrated TLAFs, the absolute value of the broad maxima, C_m^{max} , is expected to be $0.22R$, where R is the gas constant [65, 66]. The measured value, $C_m^{\text{max}} = 0.23R$, for TiYbSe_2 agrees well with this prediction [inset Fig. 4(b)].

The magnetic entropy (S_m) [Fig. 4(c) (right y-axis)] was calculated by integrating C_m/T from 70 mK upwards using the expression

$$S_m(T) = \int_{0.07 \text{ K}}^T \frac{C_m(T')}{T'} dT'. \quad (2)$$

The S_m reaches $\simeq 5.66$ J/mol K at ~ 25 K, which is nearly 98% of $R \ln 2$, confirming that Yb^{3+} ions remain in a Kramers doublet ground state with an effective spin-1/2, as expected.

The zero-field heat capacity divided by temperature, C/T , after subtracting the phonon contribution, is shown in Fig. 4(c) (left y-axis). Below 300 mK, an upturn in C/T is observed, attributed to a nuclear Schottky contribution—common in Yb-based systems at very low temperatures [26, 67]. The data below 350 mK is fitted with the expression $C(T) = \alpha/T^2 + \gamma T^b$, where

the first term represents the nuclear Schottky contribution, and the second term reflects the intrinsic low-temperature behavior of the specific heat. The fit yields $\alpha = 4.468(75) \times 10^{-4}$ JK/mol, $\gamma = 0.62(1)$ J/mol K², and $b = 1.01(1)$. The linear ($b \simeq 1$) temperature dependence of the second term suggests the possibility of a gapless QSL ground state.

Finally, we discuss the spin glass transition observed around ~ 30 mK. From the data above, our entropy calculations indicate that $\sim 98\%$ of the total magnetic entropy is released by 70 mK, leaving minimal residual entropy below this temperature. A spin glass transition, albeit to a lesser extent than a magnetic LRO, is also expected to contribute significantly to the entropy release [68]. Hence, in TiYbSe_2 , additional intrinsic magnetic features below 70 mK are unlikely; the spin glass behavior is likely driven by the presence of the residual $\sim 3\%$ free spins in the system, such as those present at the surface of the grains of the polycrystalline sample. This situation parallels the glassy transition from the free spins observed in the disorder-free Dirac QSL candidate $\text{YbZn}_2\text{GaO}_5$ [69]. Our findings argue against the possibility of a spin-glass phase and suggest that the ground state of TiYbSe_2 remains dynamic down to 20 mK.

Overall, the linear regime in heat-capacity combined with the TiYbSe_2 lacks the 120° ordered phase at zero-field down to 20 mK places this compound close to the quantum critical regime and as a prime candidate for exploring thermally assisted QSL behavior at low fields below 350 mK.

III. CONCLUSIONS

Our study reveals that TiYbSe_2 exhibits a disordered ground state at zero field down to 20 mK. A spin-glass transition is observed around ~ 30 mK, likely driven by free spins in the system. As far as we know, AC magnetization measurements in other members of this family of compounds, some of which even show a higher percentage of free spins, have not yet been conducted below 50 mK. Thus, a systematic investigation of similar spin-glass behavior in related materials could be useful. TiYbSe_2 undergoes a field-induced magnetic LRO, consistent with other members of this family, but with an enhanced exchange interaction and a correspondingly higher saturation field. Even though our measurements were performed on powder samples, the near-identical nature of the phase diagram to other members of the family suggests a similar Hamiltonian with strong isotropic Heisenberg terms, which are required for ideal geometric frustration. Additionally, the zero-field heat capacity data reveal a broad anomaly between 2–5 K, indicative of short-range spin correlations, alongside a linear temperature dependence below 350 mK. These features, combined with the absence of long-range order, especially the 120° phase at low temperatures and low fields, position TiYbSe_2 as a strong candidate for hosting a QSL ground

state. Our results open the path towards future studies on single crystals, including a detailed neutron scattering investigation of the low-energy excitations that will be crucial for investigating potential fractionalized excitations and quasiparticle states.

ACKNOWLEDGMENTS

We thank J. Xing for the fruitful discussions. A.U. gratefully acknowledges Prof. D. D. Sarma for his continued support and valuable discussions. B.P.B., A.B., and the research as a whole is supported by the U.S. Department of Energy – Office of Science, Basic Energy Sciences (Grant No. DE-SC0022986), under

the project ”*Seeking Quasiparticles from Low-Energy Spin Dynamics*.” A.U. acknowledges financial support from the Department of Science and Technology (DST), Government of India, through the DST Inspire Faculty Fellowship (Ref. No. DST/INSPIRE/04/2019/001664), as well as from the Quantum Science Center, a National Quantum Initiative Science Research Center funded by the U.S. Department of Energy. Part of this work was conducted at the National High Magnetic Field Laboratory, supported by the National Science Foundation (Cooperative Agreement No. DMR-2128556*) and the State of Florida. B.P.B. acknowledges the Quantum Design Winter School, where milli-Kelvin specific heat capacity data were collected.

-
- [1] P. W. Anderson, *Mater. Res. Bull.* **8**, 153 (1973).
 - [2] L. Balents, *Nature* **464**, 199 (2010).
 - [3] L. Savary and L. Balents, *Rep. Prog. Phys.* **80**, 016502 (2016).
 - [4] J. Knolle and R. Moessner, *Annu. Rev. Condens. Matter Phys.* **10**, 451 (2019).
 - [5] Y. Zhou, K. Kanoda, and T.-K. Ng, *Rev. Mod. Phys.* **89**, 025003 (2017).
 - [6] C. Broholm, R. Cava, S. Kivelson, D. Nocera, M. Norman, and T. Senthil, *Science* **367**, eaay0668 (2020).
 - [7] Y. Li, G. Chen, W. Tong, L. Pi, J. Liu, Z. Yang, X. Wang, and Q. Zhang, *Phys. Rev. Lett.* **115**, 167203 (2015).
 - [8] M. M. Bordelon, C. Liu, L. Posthuma, P. Sarte, N. Butch, D. M. Pajerowski, A. Banerjee, L. Balents, and S. D. Wilson, *Phys. Rev. B* **101**, 224427 (2020).
 - [9] T. Arh, B. Sana, M. Pregelj, P. Khuntia, Z. Jagličić, M. Le, P. Biswas, P. Manuel, L. Mangin-Thro, A. Ozarowski, et al., *Nat. Mater.* **21**, 416 (2022).
 - [10] Y. Shimizu, K. Miyagawa, K. Kanoda, M. Maesato, and G. Saito, *Phys. Rev. Lett.* **91**, 107001 (2003).
 - [11] J. Helton, K. Matan, M. Shores, E. Nytko, B. Bartlett, Y. Yoshida, Y. Takano, A. Suslov, Y. Qiu, J.-H. Chung, et al., *Phys. Rev. Lett.* **98**, 107204 (2007).
 - [12] T.-H. Han, J. S. Helton, S. Chu, D. G. Nocera, J. A. Rodriguez-Rivera, C. Broholm, and Y. S. Lee, *Nature* **492**, 406 (2012).
 - [13] Z. Feng, Z. Li, X. Meng, W. Yi, Y. Wei, J. Zhang, Y.-C. Wang, W. Jiang, Z. Liu, S. Li, et al., *Chin. Phys. Lett.* **34**, 077502 (2017).
 - [14] A. Banerjee, C. Bridges, J.-Q. Yan, A. Aczel, L. Li, M. Stone, G. Granroth, M. Lumsden, Y. Yiu, J. Knolle, et al., *Nat. Mater.* **15**, 733 (2016).
 - [15] Z. Meng, T. Lang, S. Wessel, F. Assaad, and A. Muramatsu, *Nature* **464**, 847 (2010).
 - [16] Y. Li, *Adv. Quantum Technol.* **2**, 1900089 (2019).
 - [17] J. Wen, S.-L. Yu, S. Li, W. Yu, and J.-X. Li, *npj Quantum Mater.* **4**, 12 (2019).
 - [18] Z. Zhu, P. Maksimov, S. R. White, and A. Chernyshev, *Phys. Rev. Lett.* **119**, 157201 (2017).
 - [19] M. R. Norman, *Rev. Mod. Phys.* **88**, 041002 (2016).
 - [20] P. Song, K. Zhu, F. Yang, Y. Wei, L. Zhang, H. Yang, X.-L. Sheng, Y. Qi, J. Ni, S. Li, et al., *Phys. Rev. B* **103**, L241114 (2021).
 - [21] Y. Tokiwa, S. Bachus, K. Kavita, A. Jesche, A. A. Tsirlin, and P. Gegenwart, *Commun. Mater.* **2**, 42 (2021).
 - [22] J. Xing, L. D. Sanjeewa, A. F. May, and A. S. Sefat, *APL Materials* **9** (2021).
 - [23] M. Xie, W. Zhuo, Y. Cai, Z. Zhang, and Q. Zhang, *Chin. Phys. Lett.* **41**, 117505 (2024).
 - [24] A. Scheie, E. Ghioldi, J. Xing, J. Paddison, N. Sherman, M. Dupont, L. Sanjeewa, S. Lee, A. Woods, D. Abernathy, et al., *Nature Physics* **20**, 74 (2024).
 - [25] M. M. Bordelon, E. Kenney, C. Liu, T. Hogan, L. Posthuma, M. Kavand, Y. Lyu, M. Sherwin, N. P. Butch, C. Brown, et al., *Nature Physics* **15**, 1058 (2019).
 - [26] K. Ranjith, S. Luther, T. Reimann, B. Schmidt, P. Schlender, J. Sichelschmidt, H. Yasuoka, A. Strydom, Y. Skourski, J. Wosnitza, et al., *Phys. Rev. B* **100**, 224417 (2019).
 - [27] A. Scheie, Y. Kamiya, H. Zhang, S. Lee, A. Woods, M. Ajeesh, M. Gonzalez, B. Bernu, J. Villanova, J. Xing, et al., *Phys. Rev. B* **109**, 014425 (2024).
 - [28] Z. Zhang, X. Ma, J. Li, G. Wang, D. Adroja, T. Perring, W. Liu, F. Jin, J. Ji, Y. Wang, et al., *Phys. Rev. B* **103**, 035144 (2021).
 - [29] Z. Zhang, J. Li, M. Xie, W. Zhuo, D. Adroja, P. J. Baker, T. Perring, A. Zhang, F. Jin, J. Ji, et al., *Phys. Rev. B* **106**, 085115 (2022).
 - [30] N. Li, M. Xie, Q. Huang, Z. Zhuo, Z. Zhang, E. Choi, Y. Wang, H. Liang, Y. Sun, D. Wu, et al., *Phys. Rev. B* **110**, 224414 (2024).
 - [31] J. Xing, L. D. Sanjeewa, J. Kim, G. Stewart, A. Podlesnyak, and A. S. Sefat, *Phys. Rev. B* **100**, 220407 (2019).
 - [32] L. Ding, P. Manuel, S. Bachus, F. Grubler, P. Gegenwart, J. Singleton, R. D. Johnson, H. C. Walker, D. T. Adroja, A. D. Hillier, et al., *Phys. Rev. B* **100**, 144432 (2019).
 - [33] K. Ranjith, D. Dmytriieva, S. Khim, J. Sichelschmidt, S. Luther, D. Ehlers, H. Yasuoka, J. Wosnitza, A. A. Tsirlin, H. Kühne, et al., *Phys. Rev. B* **99**, 180401 (2019).
 - [34] M. Baenitz, P. Schlender, J. Sichelschmidt, Y. Onyukienko, Z. Zangeneh, K. Ranjith, R. Sarkar, L. Hozoi, H. Walker, J.-C. Orain, et al., *Phys. Rev. B* **98**, 220409 (2018).
 - [35] R. Sarkar, P. Schlender, V. Grinenko, E. Haeussler, P. J. Baker, T. Doert, and H.-H. Klauss, *Phys. Rev. B* **100**,

- 241116 (2019).
- [36] T. Xie, J. Xing, S. Nikitin, S. Nishimoto, M. Brando, P. Khanenko, J. Sichelschmidt, L. Sanjeeva, A. S. Sefat, and A. Podlesnyak, arXiv preprint arXiv:2106.12451 (2021).
 - [37] P.-L. Dai, G. Zhang, Y. Xie, C. Duan, Y. Gao, Z. Zhu, E. Feng, Z. Tao, C.-L. Huang, H. Cao, et al., Phys. Rev. X **11**, 021044 (2021).
 - [38] A. Kitaev, Ann. Phys. **321**, 2 (2006).
 - [39] J. Rodríguez-Carvajal, Physica B: Condensed Matter **192**, 55 (1993).
 - [40] M. Duczmal and L. Pawlak, Journal of Alloys and Compounds **225**, 181 (1995).
 - [41] See the Supplemental Material below the reference section.
 - [42] G. Hester, H. Nair, T. Reeder, D. Yahne, T. DeLazzer, L. Berges, D. Ziat, J. Neilson, A. A. Aczel, G. Sala, et al., Phys. Rev. Lett. **123**, 027201 (2019).
 - [43] J. A. Paddison, M. Daum, Z. Dun, G. Ehlers, Y. Liu, M. B. Stone, H. Zhou, and M. Mourigal, Nature Physics **13**, 117 (2017).
 - [44] Y. Li, H. Liao, Z. Zhang, S. Li, F. Jin, L. Ling, L. Zhang, Y. Zou, L. Pi, Z. Yang, et al., Scientific reports **5**, 16419 (2015).
 - [45] U. Arjun, K. M. Ranjith, A. Jesche, F. Hirschberger, D. Sarma, and P. Gegenwart, Phys. Rev. Appl. **20**, 014013 (2023), URL <https://link.aps.org/doi/10.1103/PhysRevApplied.20.014013>.
 - [46] U. Arjun, K. M. Ranjith, A. Jesche, F. Hirschberger, D. D. Sarma, and P. Gegenwart, Phys. Rev. B **108**, 224415 (2023), URL <https://link.aps.org/doi/10.1103/PhysRevB.108.224415>.
 - [47] C. Kittel, *Introduction to Solid State Physics* (John Wiley & Sons, Inc., New York, 1986), 6th ed.
 - [48] S. Thamban, U. Arjun, M. Padmanabhan, and R. Nath, J. Phys. Condens. Matter **29**, 255801 (2017), URL <https://dx.doi.org/10.1088/1361-648X/aa6ecb>.
 - [49] S. Lee, A. J. Woods, M. Lee, S. Zhang, E. S. Choi, A. Scheie, D. Tennant, J. Xing, A. Sefat, and R. Movshovich, Phys. Rev. B **109**, 155129 (2024).
 - [50] R. Chen, H. Ju, H.-C. Jiang, O. A. Starykh, and L. Balents, Phys. Rev. B **87**, 165123 (2013).
 - [51] A. Honecker, J. Schulenburg, and J. Richter, Journal of Physics: Condensed Matter **16**, S749 (2004).
 - [52] A. Syromyatnikov, Annals of Physics **454**, 169342 (2023).
 - [53] M. Lee, E. Choi, X. Huang, J. Ma, C. Dela Cruz, M. Matsuda, W. Tian, Z. Dun, S. Dong, and H. Zhou, Phys. Rev. B **90**, 224402 (2014).
 - [54] H. Tsujii, C. Rotundu, T. Ono, H. Tanaka, B. Andraka, K. Ingersent, and Y. Takano, Phys. Rev. B **76**, 060406 (2007).
 - [55] A. Smirnov, H. Yashiro, S. Kimura, M. Hagiwara, Y. Narumi, K. Kindo, A. Kikkawa, K. Katsumata, A. Y. Shapiro, and L. Demianets, Phys. Rev. B **75**, 134412 (2007).
 - [56] M. Lee, E. Choi, J. Ma, R. Sinclair, C. D. Cruz, and H. Zhou, Mater. Res. Bull. **88**, 308 (2017).
 - [57] Y. Gao, Y.-C. Fan, H. Li, F. Yang, X.-T. Zeng, X.-L. Sheng, R. Zhong, Y. Qi, Y. Wan, and W. Li, npj Quantum Materials **7**, 89 (2022).
 - [58] J. Hwang, E. Choi, F. Ye, C. Dela Cruz, Y. Xin, H. Zhou, and P. Schlottmann, Phys. Rev. Lett. **109**, 257205 (2012).
 - [59] L. Seabra, T. Momoi, P. Sindzingre, and N. Shannon, Phys. Rev. B **84**, 214418 (2011).
 - [60] K. Ishida, M. Morishita, K. Yawata, and H. Fukuyama, Phys. Rev. Lett. **79**, 3451 (1997).
 - [61] V. Elser, Phys. Rev. Lett. **62**, 2405 (1989).
 - [62] R. Rawl, L. Ge, H. Agrawal, Y. Kamiya, C. Dela Cruz, N. Butch, X. Sun, M. Lee, E. Choi, J. Oitmaa, et al., Phys. Rev. B **95**, 060412 (2017).
 - [63] Y. Cui, J. Dai, P. Zhou, P. Wang, T. Li, W. Song, J. Wang, L. Ma, Z. Zhang, S. Li, et al., Phys. Rev. Materials **2**, 044403 (2018).
 - [64] L. Chen, D.-W. Qu, H. Li, B.-B. Chen, S.-S. Gong, J. Von Delft, A. Weichselbaum, and W. Li, Phys. Rev. B **99**, 140404 (2019).
 - [65] N. Elstner, R. Singh, and A. Young, Phys. Rev. Lett. **71**, 1629 (1993).
 - [66] B. Bernu and G. Misguich, Phys. Rev. B **63**, 134409 (2001).
 - [67] A. Steppke, M. Brando, N. Oeschler, C. Krellner, C. Geibel, and F. Steglich, Phys. Status Solidi B **247**, 737 (2010).
 - [68] J. A. Mydosh, Reports on Progress in Physics **78**, 052501 (2015), URL <https://dx.doi.org/10.1088/0034-4885/78/5/052501>.
 - [69] R. Bag, S. Xu, N. E. Sherman, L. Yadav, A. I. Kolesnikov, A. A. Podlesnyak, E. S. Choi, I. Da Silva, J. E. Moore, and S. Haravifard, Phys. Rev. Lett. **133**, 266703 (2024).
 - [70] M. Mitric, B. Antic, M. Balanda, D. Rodic, and M. L. Napijalo, J. Condens. Matter Phys. **9**, 4103 (1997).
 - [71] S. Mugiraneza and A. M. Hallas, Commun. Phys. **5**, 95 (2022).

Supplemental Material

1. Two-level fitting of DC magnetization

At $T < 100$ K, $1/\chi(T)$ data deviates from the Curie-Weiss behavior and a clear change in slope is observed in the data [see Fig. 5]. This deviation likely arises from the thermal depopulation of excited crystal electric field (CEF) levels. Even though, to get a clear understanding of CEF level, other experiments like neutron scattering or Raman spectroscopy are needed, we can roughly estimate the effect of excited crystal field levels using the two-level approximation [45, 46, 70, 71]:

$$(\chi - \chi_0)^{-1} = 8(T - \theta_{CW}) \frac{1 + \exp(-\frac{\Delta}{T})}{\mu_{\text{eff},0}^2 + \mu_{\text{eff},1}^2 \exp(-\frac{\Delta}{T})}. \quad (3)$$

Here, Δ is the energy splitting to the first excited crystal field level, with an effective moment of $\mu_{\text{eff},1}$, while $\mu_{\text{eff},0}$ is the effective moment of the crystal field ground state. A fit to the $1/(\chi - \chi_0)$ data in the range 25 – 300 K yields $\Delta \simeq 127$ K, $\mu_{\text{eff},0} \simeq 3.9 \mu_B$, $\mu_{\text{eff},1} \simeq 6.0 \mu_B$, and $\theta_{CW} \simeq -33$ K. The obtained θ_{CW} is significantly reduced compared to θ_{CW}^{HT} from the high-temperature Curie-Weiss fitting. Below 25 K, deviation of the fit from the data indicates that $\mu_{\text{eff},0}$ and θ_{CW} do not fully describe the lowest Kramers doublet. Extending the model to include all CEF levels is challenging due to the large number of adjustable parameters required.

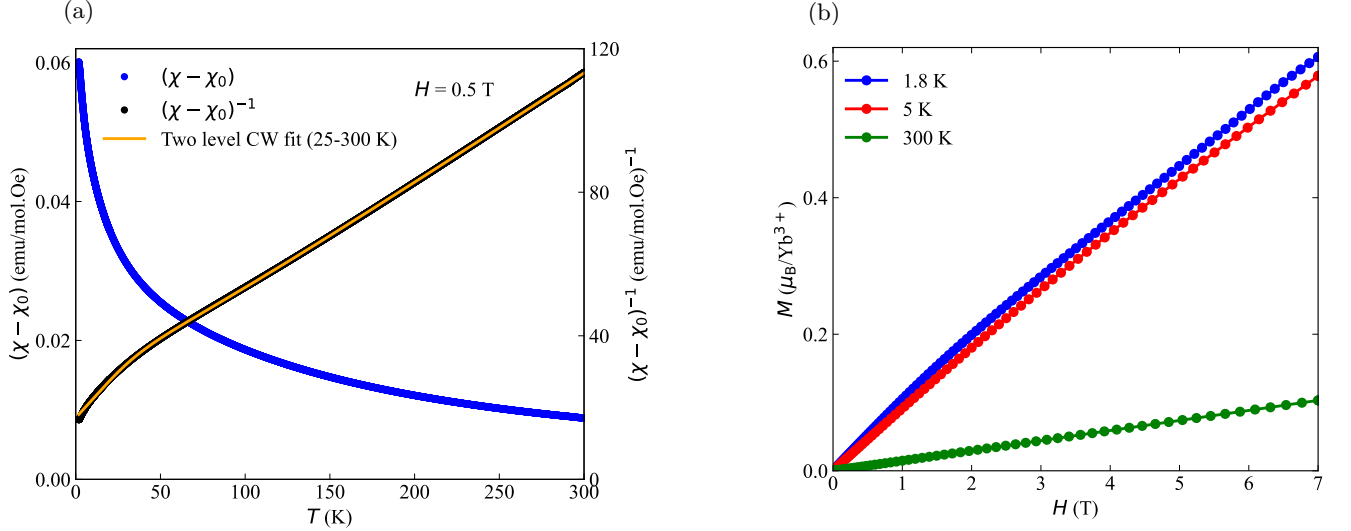


FIG. 5. (a) Temperature-dependent DC magnetic susceptibility, $\chi(T)$ [left y-axis], and inverse magnetic susceptibility, $1/\chi(T)$ [right y-axis], at 0.5 T with two-level CW fit. (b) Magnetization as a function of field, $M(H)$, at different temperatures.

2. AC magnetization

Fig. 6(a) shows zero-field $\chi'(T)$ measured down to 20 mK using a dilution refrigerator, revealing a frequency-dependent peak near ~ 35 mK. This behavior is indicative of a spin-glass-like transition, likely originating from orphan spins present in the powder sample. The red arrow highlights the shift in the glassy transition temperature with frequency. In the main text, for clarity, we have shown data only in the 20 – 50 mK range. The inset displays zero-field $\chi'(T)$ measured down to 300 mK using a ^3He insert, where no spin freezing is observed. Overall, no spin freezing is seen down to 50 mK, consistent with other compounds in this material family. The glassy transition appears only when measurements are performed below 50 mK—a temperature range that, to the best of our knowledge, has not been previously explored in AC susceptibility measurements.

Fig. 6(b) shows $\chi'(T)$ collected under various high magnetic fields, where the system enters a magnetically ordered state. These curves represent the raw data without any vertical offsets. In the main text, for clarity in identifying transition temperatures, each curve is vertically shifted by unequal offsets.

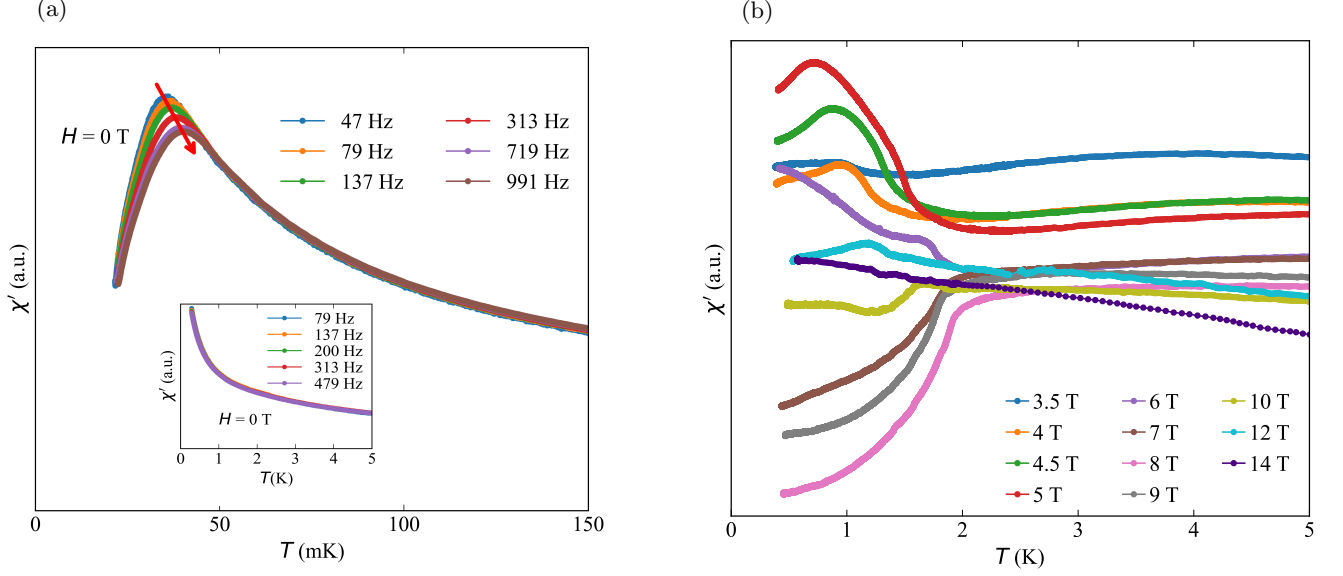


FIG. 6. (a) Zero-field $\chi'(T)$ measured down to 20 mK using a dilution refrigerator, shows a frequency-dependent peak near ~ 35 mK, indicative of a spin-glass-like transition, likely originating from orphan spins in the powder sample. The red arrow highlights the shift in the glassy transition temperature with frequency. The inset shows zero-field $\chi'(T)$ measured down to 300 mK using a ^3He insert, where no spin freezing is observed. (b) $\chi'(T)$ measured under various high magnetic fields, where the system is in a magnetically ordered state. These curves represent the raw data without any vertical offsets.

3. Low temperature specific heat data fit

Specific heat, $C(T)$, data below 350 mK is fitted using equation $\alpha/T^2 + \gamma T^b$, as shown in Fig. 7(a). Here, $C(T)$ represents the specific heat capacity after subtracting the phonon contribution. The fit yields $\gamma = 0.62(1)\text{J/molK}^2$, $b = 1.01(1)$, and $\alpha = 4.468(75) \times 10^{-4}\text{JK/mol}$. The value of α obtained from this fit is used to estimate the nuclear contribution to the heat capacity, C_{nuc} , as shown in the main text Fig. 4(c). After subtracting C_{nuc} , the magnetic heat capacity, C_{m} , exhibits a linear temperature dependence as shown in Fig. 7(b).

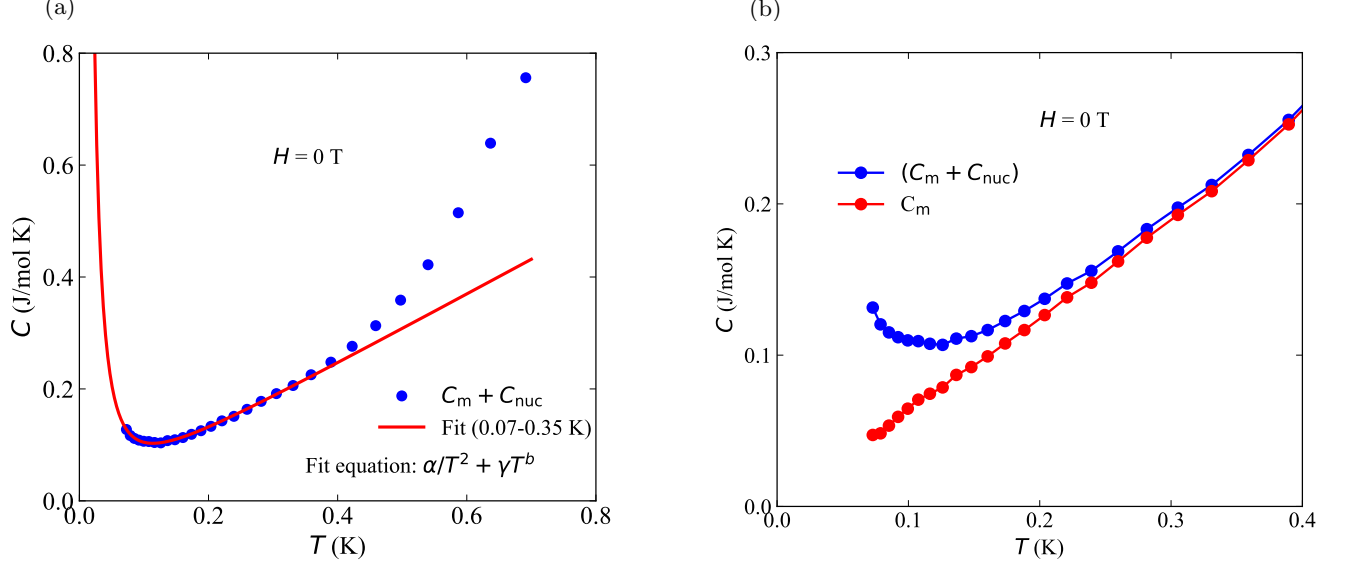


FIG. 7. (a) Zero-field specific heat, $C(T)$, fitted with the equation $\alpha/T^2 + \gamma T^b$ in the temperature range of 70-350 mK. (b) Magnetic heat capacity, $C_{\text{m}}(T)$, obtained after subtracting the nuclear contribution, $C_{\text{nuc}}(T)$. In the main text, C_{m}/T is presented. This plot clearly demonstrates the linear temperature dependence of C_{m} .

4. Field-dependent specific heat capacity

Fig. 8 presents the $C_m(T)$ data measured down to 1.8 K under different applied magnetic fields. Sharp peaks begin to emerge below 2 K starting from 6 T, clearly indicating a field-induced magnetic phase transition. This observation supports the results obtained from AC and DC magnetization measurements. Notably, the upturn in $C_m(T)$ at 8 T begins at a higher temperature compared to other fields, suggesting that the transition temperature reaches its maximum at ~ 8 T, which is consistent with the $\chi'(T)$ results.

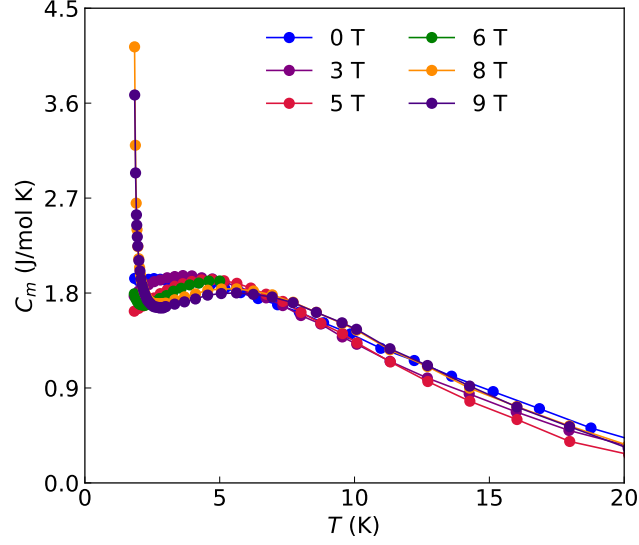


FIG. 8. Magnetic heat capacity, $C_m(T)$, measured under different applied magnetic fields down to 1.8 K.